Available online at www.sciencedirect.com
ScienceDirect
Journal of Sound and Vibration 304 (2007) 677–690
JOURNAL OF SOUND AND VIBRATION
www.elsevier.com/locate/jsvi

Direct numerical simulations of trailing-edge noise generated by boundary-layer instabilities

R.D. Sandberg[a,*], N.D. Sandham[a], P.F. Joseph[b]

[a]*Aerodynamics and Flight Mechanics Research Group, School of Engineering Sciences, University of Southampton, Southampton SO17 1BJ, UK*
[b]*Institute of Sound and Vibration Research, University of Southampton, Southampton SO17 1BJ, UK*

Received 25 May 2006; received in revised form 8 February 2007; accepted 6 March 2007
Available online 26 April 2007

Abstract

Direct numerical simulations (DNS) are conducted of noise generated at an infinitely thin trailing edge (TE). The aim is to predict the far-field sound and the near-field hydrodynamics, thereby providing an insight into the physical mechanisms of sound generation at airfoil TEs and potentially helping to validate acoustic theories. One of the theories widely used is the classical inviscid theory of Amiet, where the far-field sound can be evaluated in closed form if the convecting surface pressure spectrum upstream of the TE is known. For the first time, data from DNS including viscous effects are compared to the classical inviscid TE noise theory. In the present investigation, Tollmien–Schlichting waves are introduced close to the inflow boundary. The disturbances propagate downstream producing pressure fluctuations at the TE. In conducting two-dimensional DNS the theoretical method requires modification to account for the radiation of the total pressure difference in two dimensions only, as opposed to the three-dimensional sound radiation originally considered by Amiet. The modified theoretical analysis and a comparison between DNS and theoretical results are presented, scrutinizing the assumptions made in the derivation. Amiet's surface pressure jump transfer function is found to predict the scattered pressure field accurately. Directivity plots of DNS data show that viscous effects appear to smear individual lobes and that a downstream pointing lobe is present at higher Mach number which is attributed to an additional wake source.

1. Introduction

Noise generated by turbulent flow over trailing edges (TEs) is an important aspect in the design of quieter airplanes and propulsion systems as it contributes to airframe noise, fan noise and other sources of sound. The acoustic analogy developed by Lighthill [1,2] states that turbulent fluctuations in free space are inefficient radiators of noise in low-speed flows. Due to the quadrupole-type character of turbulent fluctuations the radiated acoustic intensity scales as M^8. In the presence of solid boundaries, surface dipoles lead to a M^6 scaling as predicted by Curle [3]. However, when a turbulent eddy passes a sharp edge of a solid body, the turbulent fluctuations radiate even more strongly (M^5-scaling), as shown by Ffowcs Williams and Hall [4]. Therefore, due to this scaling, in the absence of significant other generating mechanisms, such as ingestion of

*Corresponding author. Tel.: +44 23 80597386.
E-mail address: sandberg@soton.ac.uk (R.D. Sandberg).

0022-460X/$ - see front matter © 2007 Elsevier Ltd. All rights reserved.
doi:10.1016/j.jsv.2007.03.011

Nomenclature

A_{dist}	amplitude of disturbance
b	semi-chord
c	speed of sound
$C, K, T, \mathbf{Y}_i$	transformation variables
d	half-span
E	total energy $E = T/[\gamma(\gamma-1)M^2 + 0.5\mathbf{u_i u_i}$
E^*	Fresnel integral
f_i	scaling of incident pressure field
$\mathbf{F_i}$	forcing term
g_2	two-dimensional Green's function in time domain
G_2	two-dimensional Green's function
$H_\nu^{(2)}$	νth order Hankel function of the second kind
H_D, H_S	surface pressure jump transfer function
K_x	non-dimensional wavenumber $K_x = \omega b/U_c$
M	Mach number
p	pressure
Pr	Prandtl number
$\mathbf{q_k}$	heat-flux vector
R	$\sqrt{(y_1-x_1)^2 + \beta^2(y_2-x_2)^2}$
R_d	$\sqrt{x_1^2 + x_2^2}$
Re	Reynolds number
t	time
T	temperature
$\mathbf{u_i}$	velocity vector
U, U_c	streamwise freestream velocity, convection speed
$\mathbf{x_i}, \mathbf{y_i}$	coordinates normalized with b

Greek letters

β	$\sqrt{1-M^2}$
δ	Dirac delta function
δ^*	displacement thickness
$\delta_{\mathbf{ik}}$	Kronecker operator
Δp	pressure difference between top and bottom surface
ε	convergence factor
γ	ratio of specific heats
Γ, Ω	transformation variables
μ	molecular viscosity
μ_0	reduced frequency $\mu_0 = \omega b/(c\beta^2)$
ρ	density
σ	$\sqrt{x_1^2 + \beta^2 x_2^2}$
$\tau_{\mathbf{ik}}$	stress tensor
ω	frequency
ξ	integration variable

Subscripts

$1, 2$	indices for streamwise and wall-normal directions
i	incident
i, j, k	indices for Cartesian tensor notation
s	scattered
t	total

turbulence, formation of tip-vortices, etc., TEs are one of the most significant sources of sound, particularly at low Mach numbers.

A review of TE theories was conducted by Howe [5]. He identified three categories, namely (i) theories based on Lighthill's acoustic analogy, (ii) theories based on the solution of special problems approximated by linearized equations, and (iii) ad hoc models. Howe concluded that all methods, when interpreted properly, essentially gave the same results. The theoretical results were supported by TE noise experiments on a NACA0012 airfoil [6]. Out of the second category, the theory of Amiet [7] appears to be an attractive approach as the far-field noise can be predicted with the convecting surface pressure spectrum upstream of the TE as the required input rather than having to provide the turbulence quadrupole sources in full.

With the recent dramatic growth in computing power, conducting numerical simulations in order to compute aerodynamically generated sound has become increasingly feasible. Solving the full unsteady Navier–Stokes equations to directly compute both the far-field sound and the near-field hydrodynamics is desirable. The use of direct numerical simulations (DNS) avoids difficulties with hybrid approaches, such as the coupling of different numerical methods, storage of intermediate data [8], and the sensitivity to the position of integration surfaces [9]. Also, uncertainties with using subgrid-stress models for the small-scale structures in LES [10,11] are eliminated. Thus, DNS can provide an insight into the physical mechanisms of

sound generation and potentially help to validate acoustic theories. Here, DNS of TE noise are conducted to evaluate the inviscid theory of Amiet [7]. Amiet's classical theory was derived for flow past a flat plate. Therefore, an infinitely thin plate with a laminar boundary layer on each side is considered. In order to generate a surface pressure difference, Tollmien–Schlichting (TS) waves are introduced on the top side of the flat plate close to the inflow boundary. The instability waves convect downstream and pass the sharp TE, generating TE noise. An additional motivation for using TS waves is the observation of boundary-layer instability noise on airfoils. Tonal noise from airfoil TEs was already observed in the 1970s [12,13] and more recently Nash et al. [14] were able to link tonal noise in airfoil experiments to boundary layer instabilities. The paper presents the first DNS that have been conducted of boundary layer instability waves convecting over an infinitely thin TE, providing data containing the effects of viscosity that are used to scrutinize the classical inviscid theory of Amiet.

To allow for parametric studies, DNS are conducted in two dimensions. Amiet's theory considers three-dimensional (3-D) sound radiation, hence a modification of Amiet's theory accounting for two-dimensional (2-D) sound radiation is derived. The modified theoretical analysis is presented and comparisons between theoretical results and DNS data are made, scrutinizing the assumptions made in the derivation. For the present investigation, a high-order accurate numerical method is chosen which is free of upwinding, artificial dissipation or any form of explicit filtering.

2. Governing equations

2.1. Theoretical approach

The classical theory of Amiet [7] is valid for compressible flow and assumes a pressure pattern on the airfoil surface which convects past the TE, producing a radiating pressure field of similar magnitude. Amiet's theory considers 3-D sound radiation. In the current investigation, 2-D laminar flows with single-frequency disturbances are investigated. Therefore, a modification of Amiet's theory accounting for 2-D sound radiation of single-frequency disturbances is derived in the coordinate system $\mathbf{x} = [x_1, x_2]^{\mathrm{T}}$, where x_1 and x_2 are the streamwise and the wall normal directions non-dimensionalized with the semi-chord b, respectively. A plate with zero thickness is assumed to be semi-infinite, i.e. the leading edge is not considered. However, the integration of the sources along the plate coordinate y_1 is conducted over a finite length, namely $-2 \leqslant y_1 \leqslant 0$. Goldstein's formulation [15] of the acoustic analogy, which represents the fundamental equation governing the generation of aerodynamic sound in the presence of solid boundaries in a moving reference frame, is used as the starting point. Neglecting viscosity and performing a Fourier transform in time yields the acoustic pressure at a single frequency

$$p(\mathbf{x}, \omega) = -\int_{-2}^{0} \Delta p_t(\mathbf{y}, \omega) \frac{\partial}{\partial y_2} G_2(\mathbf{x}, \mathbf{y}, \omega)\, \mathrm{d}y_1. \tag{1}$$

Eq. (1) is derived for a moving reference frame. Here, the sources and the observer are fixed while the flow moves downstream. Therefore, the Green's function G_2 needs to be a solution for the wave equation with mean flow

$$\left[\beta^2 \frac{\partial^2}{\partial y_1^2} + \frac{\partial^2}{\partial y_2^2} - \frac{1}{c^2}\frac{\partial^2}{\partial t^2} - \frac{2U}{c^2}\frac{\partial^2}{\partial y_1 \partial t}\right] g_2(\mathbf{x}, \mathbf{y}, \tau, t) = -\delta(\mathbf{y} - \mathbf{x})\delta(t - \tau). \tag{2}$$

Performing the coordinate transformation

$$Y_1 = y_1, \quad Y_2 = \beta y_2, \quad T = \beta t + \frac{M Y_1}{\beta c}, \quad \Omega = \frac{\omega}{\beta}, \tag{3}$$

$$K = \frac{k}{\beta^2}, \quad C = c\beta$$

results in the wave equation for a stationary medium

$$\left[\frac{\partial^2}{\partial Y_1^2}+\frac{\partial^2}{\partial Y_2^2}-\frac{1}{C^2}\frac{\partial^2}{\partial T}\right]g_2(\mathbf{X},\mathbf{Y},\Gamma,T)=-\frac{1}{\beta}\,\delta(\mathbf{Y}-\mathbf{X})\delta\left(\frac{T}{\beta}-\frac{MY_1}{\beta^3 C}-\Gamma\right). \tag{4}$$

Inverting the above transformation coordinates and substituting them into the known stationary medium Green's function [16] and performing a Fourier transform in time results in the 2-D Green's function in frequency space

$$G_2(\mathbf{x},\mathbf{y},\omega)=\frac{1}{4\beta\mathbf{i}}\,H_0^{(2)}\{\omega\tau+\mu_0[M(y_1-x_1)+R]\}. \tag{5}$$

Setting the wall-normal origin of the plate to $y_2=0$, Eq. (1) can now be written as

$$p(\mathbf{x},\omega)=\frac{\mathrm{i}x_2\omega b}{4\beta c}\int_{-2}^{0}\Delta p_t(\mathbf{y},\omega)\frac{1}{R}\,H_1^{(2)}\{\mu_0[M(y_1-x_1)+R]\}\,\mathrm{d}y_1. \tag{6}$$

The total pressure difference on the surface is the sum of the incident pressure difference and the scattered pressure difference

$$\Delta p_t=\Delta p_i+\Delta p_s. \tag{7}$$

In cases where the entire time-series of the surface pressures is available (which it is for DNS) Eq. (6) can be integrated directly to obtain the acoustic pressure field. However, when only the incident pressure field is known, the total pressure field at the TE can be determined from the incident pressure field through a transfer function [17]. This is because the incident pressure on one side of the plate is equivalent to a pressure jump when no incident pressure is considered on the other side of the plate. As a prerequisite, the unsteady Kutta condition is assumed to hold at the TE, i.e. $\Delta p_t=0$, and the condition of no-flow across the plate is imposed. With the above conditions, the Schwartzschild solution can be employed to derive a surface pressure jump [17] (for incident pressure fluctuations on one side of the airfoil)

$$\begin{aligned}&\Delta p_s(y_1,K_x)=H_S(y_1,K_x)p_i(y_1,K_x)\\&\text{with}\quad H_S(y_1,K_x)=\{(1+\mathrm{i})E^*[-(\mu_0(1+M)+K_x)y_1]-1\}.\end{aligned} \tag{8}$$

The function E^* is a combination of Fresnel integrals

$$E^*(x)=\int_0^x\frac{1}{\sqrt{2\pi\xi}}\,\mathrm{e}^{-\mathrm{i}\xi}\,\mathrm{d}\xi. \tag{9}$$

Therefore, the total pressure difference becomes

$$\begin{aligned}\Delta p_t(y_1,K_x)&=H_D(y_1,K_x)p_i(y_1,K_x)\\&=[f_i(y_1,K_x)+H_S(y_1,K_x)]p_i(y_1,K_x).\end{aligned} \tag{10}$$

In Amiet's original paper [7], $f_i(y_1,K_x)$ was set to unity to account for the incident pressure. However, a convergence factor ε was subsequently introduced [18] to gradually decrease the incident pressure towards the leading edge such that $f_i(y_1,K_x)=\exp(\varepsilon K_x y_1)$. In a single frequency case, the incident pressure disturbance can be represented as

$$p_i(y_1,K_x)=p_0\mathrm{e}^{\mathrm{i}\omega(t-y_1 b/U_c)}. \tag{11}$$

Hence, analogous to Eq. (2) in Amiet's paper [7], the total pressure jump (normalized with p_0) can be evaluated as

$$\Delta p_t(y_1,K_x)=H_D(y_1,K_x)\mathrm{e}^{-\mathrm{i}K_x y_1}. \tag{12}$$

Inserting Eq. (10) into Eq. (6) yields the 2-D acoustic pressure field as a function of the incident pressure field

$$p(\mathbf{x},\omega)=\frac{\mathrm{i}x_2\omega b}{4\beta c}\int_{-2}^{0}H_D(y_1,K_x)p_i(y_1,K_x)\frac{1}{R}\,H_1^{(2)}\{\mu_0[M(y_1-x_1)+R]\}\,\mathrm{d}y_1. \tag{13}$$

Note that, in contrast to the original theory, no far-field approximation has been made.

2.2. Direct numerical simulations

The flow under consideration is governed by the full compressible Navier–Stokes equations. The fluid is assumed to be an ideal gas with constant specific heat coefficients. All quantities are made dimensionless using the flow-quantities at a reference location in the flow; here the freestream/inflow location is used. The non-dimensional continuity, momentum and the energy equations are:

$$\frac{\partial \rho}{\partial t} + \frac{\partial}{\partial x_k}(\rho \mathbf{u_k}) = 0, \tag{14}$$

$$\frac{\partial}{\partial t}(\rho \mathbf{u_i}) + \frac{\partial}{\partial x_k}[\rho \mathbf{u_i u_k} + p\delta_{\mathbf{ik}} - \tau_{\mathbf{ik}}] = \mathbf{F_i}, \tag{15}$$

$$\frac{\partial}{\partial t}(\rho E) + \frac{\partial}{\partial x_k}\left[\rho \mathbf{u_k}\left(E + \frac{p}{\rho}\right) + \mathbf{q_k} - \mathbf{u_i}\tau_{\mathbf{ik}}\right] = 0, \tag{16}$$

where $\mathbf{F_i}$ is a volume force and the total energy is defined as $E = T/[\gamma(\gamma-1)M^2] + 0.5\mathbf{u_i u_i}$. The stress tensor and the heat-flux vector are computed as

$$\tau_{\mathbf{ik}} = \frac{\mu}{Re}\left(\frac{\partial \mathbf{u_i}}{\partial x_k} + \frac{\partial \mathbf{u_k}}{\partial x_i} - \frac{2}{3}\frac{\partial \mathbf{u_j}}{\partial x_j}\delta_{\mathbf{ik}}\right), \quad \mathbf{q_k} = \frac{-\mu}{(\gamma-1)M^2 PrRe}\frac{\partial T}{\partial x_k}, \tag{17}$$

respectively, where the Prandtl number is assumed to be constant at $Pr = 0.72$, and $\gamma = 1.4$. The molecular viscosity μ is computed using Sutherland's law [19], setting the ratio of the Sutherland constant over freestream temperature to 0.36867. To close the system of equations, the pressure is obtained from the non-dimensional equation of state $p = (\rho T)/(\gamma M^2)$. In order to introduce disturbances into the boundary layers, a volume force $\mathbf{F_i}$ is added to the right-hand side of the governing equations. To minimize the sound generation of the disturbances, a solenoidal and therefore quiet forcing is used [20].

$$F_1 = \frac{\partial \phi}{\partial x_2}, \quad F_2 = -\frac{\partial \phi}{\partial x_1}, \quad \text{with} \tag{18}$$

$$\phi = A_{\text{dist}} \sin(\omega t)\left[1 - \cos\left(\frac{(x_1 - x_{1_b})\pi}{x_{1_e} - x_{1_b}}\right)\right]\left[1 - \cos\left(\frac{(x_2 - x_{2_b})\pi}{x_{2_e} - x_{2_b}}\right)\right], \tag{19}$$

with x_{i_b} and x_{i_e} being the start and end points of the forcing, respectively.

3. Numerical method

Results from DNS will be compared to theoretical results. Hence, two numerical codes are used: one solves for the acoustic pressure as a function of the surface pressure difference, while the other solves the Navier–Stokes equations. For the analytical approach Eqs. (6) or (13) are integrated using a fourth-order accurate integration. The plate is discretized with a non-uniform grid, clustering most points in the vicinity of the TE to reduce computational cost.

The compressible Navier–Stokes equations are solved using a high-order numerical scheme applicable to general geometries. The extension to general coordinates is achieved through metric terms pre-multiplying the derivatives of the governing equations. No upwinding, artificial dissipation or explicit filtering are employed. Stability is rather achieved through appropriate conditioning of the governing equations, namely an entropy-splitting approach that splits the nonlinear terms into conservative and non-conservative parts and a Laplacian formulation of the viscous and heat conduction terms. The latter is used to avoid odd–even decoupling when using central finite-difference schemes. In addition, compatible spatial difference operators for the interior and boundary points are employed. Further details on the fundamental numerical approach are given in Ref. [21]. A non-reflecting zonal boundary condition is used to avoid spurious pressure-oscillations from the boundaries, in particular the outflow boundary. The method is based on commonly used characteristic boundary conditions. Here, incoming characteristics are ramped to zero in a buffer zone as

opposed to merely setting them to zero at the boundary [22]. In contrast to most other zonal approaches, the method is free of coefficients that require calibration and only the length of the fringe zone needs to be specified.

4. Validation

To ensure that the numerical codes used in the current work produce accurate results a thorough validation was conducted of both the analytical approach and the DNS.

4.1. Analytical approach

In Amiet's original theory [7], a closed-form solution was obtained for the far-field sound spectrum. For the modified 2-D theory, the equations to be solved are only available in integral form. Therefore, the correctness of the non-equidistant integration needs to be established. Given the lack of published results for a 2-D theory, the numerical code was applied to Amiet's 3-D theory, solving

$$p(\mathbf{x},\omega)=\frac{\mathrm{i}x_2\omega b}{2\pi c\sigma^2}\int_{-2}^{0}H_D(y_1,K_x)\mathrm{e}^{-\mathrm{i}K_x y_1}\mathrm{e}^{-\mathrm{i}\mu_0 y_1(M-(x_1/\sigma))}\,\mathrm{d}y_1 \tag{20}$$

by numerically integrating over y_1. The first validation case was conducted with $M=0.05$, $\mu_0=5.0125$ and $K_x=100$. These values correspond to the parameters investigated by Roger and Moreau [23] when using '$kc=10$'. For comparison, the closed-form solution (Eq. (5)) of Amiet [7] was solved, dropping the last term to be consistent with using the convergence factor ε in $H_D(y_1,K_x)$ [18]. Fig. 1 shows the magnitude of acoustic pressure obtained from numerically integrating the 2-D and 3-D theory for two different radii R. Amiet's closed-form solution is added for comparison. The results obtained from numerically integrating Amiet's original theory and using the closed-form solution ($0^\circ\leqslant\theta\leqslant180^\circ$) match exactly, validating the numerical integration procedure. At $R_d=2$, the solution of the 2-D theory ($-180^\circ\leqslant\theta\leqslant0^\circ$) is similar in magnitude but different in shape, with all lobes pointing further upstream than in the 3-D case. This can be attributed to the fact that no far-field approximation was made in the derivation of the 2-D theory, i.e. near-field effects are included. When increasing the radius to $R_d=10$, the 2-D theory predicts a larger magnitude than 3-D theory. This was expected as the radiation is confined to two dimensions and should therefore show a smaller decay ($p\propto1/\sqrt{R_d}$ for 2-D radiation versus $p\propto1/R_d$ for 3-D radiation). The amplitude of the 2-D result is divided by 1.75 to allow for a detailed comparison of the shape with the 3-D result. For the current parameters, the difference in shape is negligible.

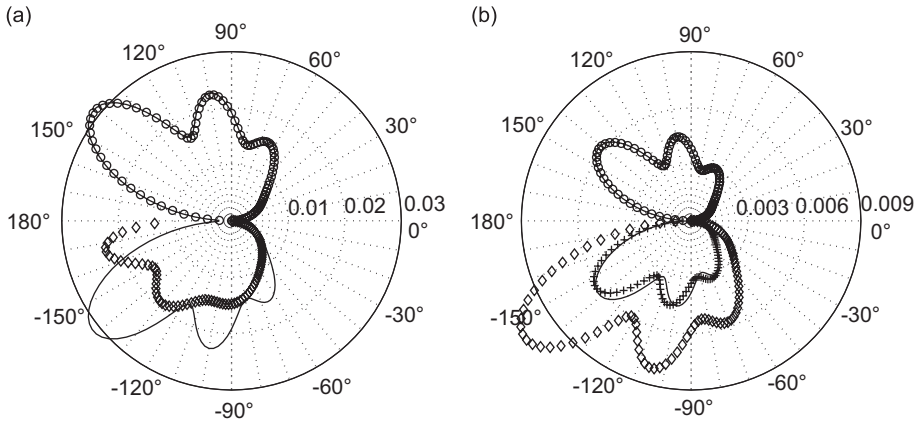

Fig. 1. Magnitude of acoustic pressure at $R_d=2$ (a) and $R_d=10$ (b); (–) closed-form solution of Amiet [7], (○) numerical integration of Amiet's 3-D theory (upper half-plane only), (◇) numerical integration of 2-D theory (lower half), (+) numerical integration of 2-D theory divided by 1.75 (lower half); $\mu_0=5.0125$, $K_x=100$ and $M=0.05$.

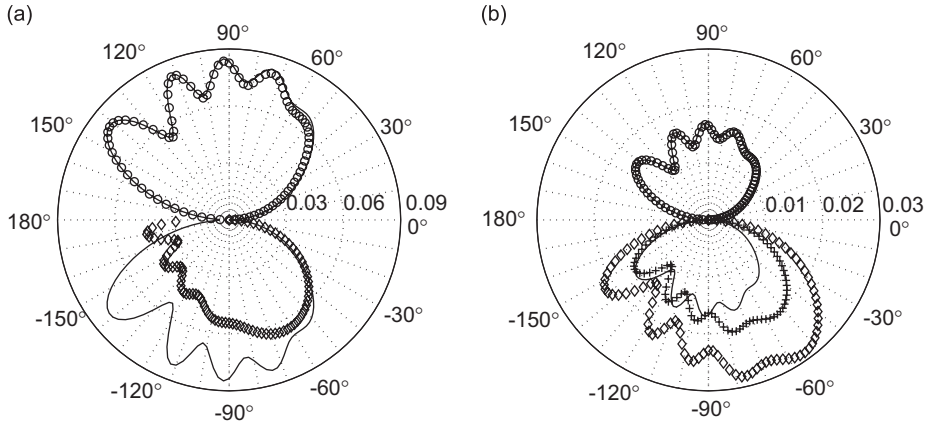

Fig. 2. Magnitude of acoustic pressure at $R_d = 2$ (a) and $R_d = 10$ (b); (–) closed-form solution of Amiet [7], (○) numerical integration of Amiet's 3-D theory (upper half-plane only), (◇) numerical integration of 2-D theory (lower half), (+) numerical integration of 2-D theory divided by 1.4 (lower half); $\mu_0 = 5.0125$, $K_x = 100$ and $M = 0.6$.

Judging from the results obtained in the far field ($R_d = 10$), the use of a strictly 2-D theory does not appear to be necessary for this low Mach number case. However, significant differences occur when increasing the Mach number. The calculations were repeated at $M = 0.6$ using the same non-dimensional parameters μ_0 and K_x. The results are shown in Fig. 2. For $R_d = 2$ the downstream pointing lobe appears to be the most significant one when employing 2-D theory. That this is not a near-field effect is demonstrated by the graph showing the results at $R_d = 10$. The amplitude of the 2-D result is again scaled to allow for a detailed comparison with the 3-D result. The lobes that are inclined in the upstream direction are highly similar to those calculated with 3-D theory. However, the downstream pointing lobe is considerably larger in amplitude. Thus not only is the magnitude increased due to the confinement of the sound field to a plane, it also appears that the radiation in the downstream direction gains in significance.

4.2. DNS code

The computation of TS waves in a flat plate zero pressure gradient boundary layer was chosen as a challenging test for validation of the DNS code. A viscous hydrodynamic instability is responsible for the growth of small amplitude waves (TS waves) in a boundary layer. Therefore, an accurate representation of the physical mechanisms in the near-wall region is crucial for capturing the correct behavior of the waves, such as phase and amplitude distributions and, in particular, the growth rates. The set-up of the calculation follows case 1 from Fasel and Konzelmann [24]. Our data are compared to linear stability theory (LST) and incompressible results [24] where a DNS code was employed and, therefore, potential deviations from LST caused by non-parallel effects were accounted for. The Mach number was set to $M = 0.25$ in order to minimize the effect of compressibility while still allowing for practical timesteps. The disturbances were introduced into the flow as described above using Eq. (18).

The amplification rate of the inner maximum of the streamwise velocity component is shown in Fig. 3 as a function of Reynolds number based on displacement thickness, Re_{δ^*}. The results obtained with the compressible Navier–Stokes code agree well with LST and the reference DNS. A larger amplification rate than that predicted by LST is found and the maximum is shifted downstream, consistent with the findings of Fasel and Konzelmann [24] when using DNS. The amplitude distribution of the streamwise velocity component at $Re_{\delta^*} = 800$ shows excellent agreement with the reference data. This demonstrates that the Navier–Stokes code is capable of accurately representing the development of hydrodynamic instabilities.

In the intended TE calculations a wake will develop downstream of the TE containing highly energetic structures. It is essential that residual pressure oscillations caused by these vortical structures crossing the

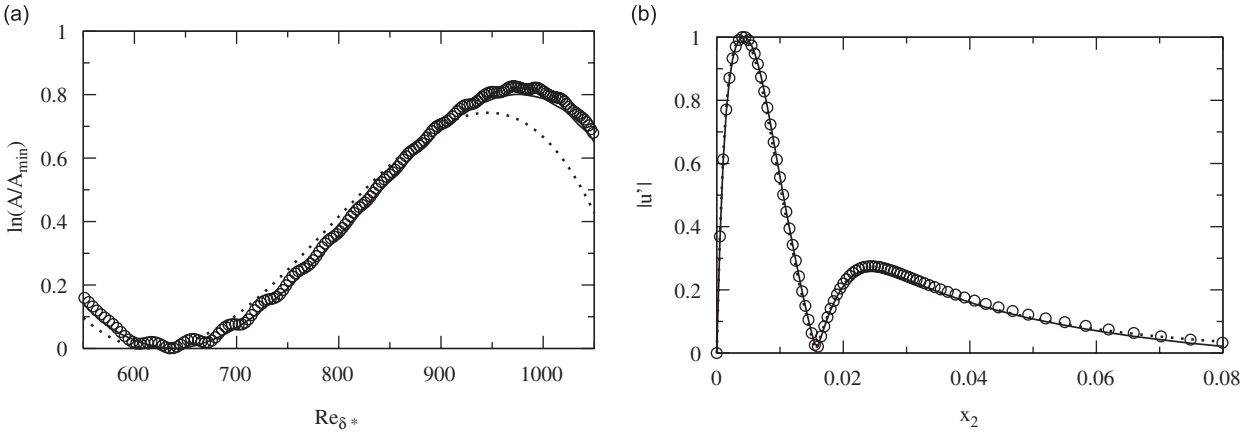

Fig. 3. Amplification rate (a) of inner maximum of streamwise velocity and amplitude distribution (b) of streamwise velocity component at $Re_{\delta^*} = 800$; (○) current compressible DNS, (···) linear stability theory, (—) incompressible reference; $M = 0.25$, $f = 2.222$.

outflow boundary are significantly reduced to avoid interference with the low amplitude sound waves produced at the TE. This motivated the development of a zonal characteristic boundary condition offering a coefficient-free and inexpensive way of drastically reducing spurious pressure oscillations. It was demonstrated that the DNS code incorporating this novel boundary treatment is suitable for simulations of the acoustic scattering of TS waves convecting over a TE [22].

5. Results

DNS of TE sound generation were conducted for two different Mach numbers. The computational domain has the dimensions $-2.286 \leqslant x_1 \leqslant 2.142$ and $-3.714 \leqslant x_2 \leqslant 3.714$ with the infinitely thin plate extending from $-2.286 \leqslant y_1 \leqslant 0$ at $y_2 = x_2 = 0$. At the TE, the top and bottom boundary layers have a displacement thickness of $\delta^* = 6.686 \times 10^{-3}$, resulting in $Re_{\delta^*} = 1170$, and the Mach number is specified at $M = 0.4$ and 0.6. 2500 and 600 non-equidistantly spaced points are used for the x_1- and x_2-direction, respectively, with the finest resolution at the TE. The surface is discretized with 620 points in the streamwise direction. Additional simulations were conducted with different domain sizes and grid resolution and did not show a difference in the results. A zonal characteristic boundary condition is used at the outflow (for $x_1 \geqslant 1.571$), and a traditional sponge employing a dissipation term is used for the upper and lower freestream boundaries ($|x_2| \geqslant 2.857$) and the inflow boundary ($-2.286 \leqslant x_1 \leqslant -2$). The simulations are first conducted without applying forcing. An unsteady wake forms downstream of the TE for both Mach numbers, shedding large vortices. Once a quasi time-periodic state is reached, time-dependent forcing is introduced at $x_1 = -2.129$ and $x_2 = 0.00286$ with $A_{\text{dist}} = 8 \times 10^{-3}$. The non-dimensional forcing frequency $\omega = 6.4\pi$ was found from LST to generate TS waves that are amplified up to the TE. The amplitude of the pressure disturbance associated with the TS wave is smaller than 1% of the mean pressure value at the TE. The reasons for choosing this amplitude are the following. The disturbance amplitude must exceed a lower threshold so that the sound field can be reliably detected at a distance from the TE. At the same time, the amplitude of the disturbances must be below the nonlinear saturation level of TS waves in order to avoid higher harmonics. The above parameters result in the non-dimensional parameters $\mu_0 = 8.38$ and $K_x = 45.11$ at $M = 0.4$, and $\mu_0 = 16.49$ and $K_x = 41.89$ at $M = 0.6$.

For an overview of the resulting flow field, instantaneous contours of dilatation are shown in Fig. 4 for both Mach numbers. The graphs reveal the unsteady wake forming downstream of the TE and the TS waves on the upper side of the singular plate. Acoustic waves generated by the scattering of the instability waves at the TE can be clearly seen. These waves radiate in both the positive and negative x_2-direction in phase opposition and exhibit a wavelength considerably greater than that of the original TS wave.

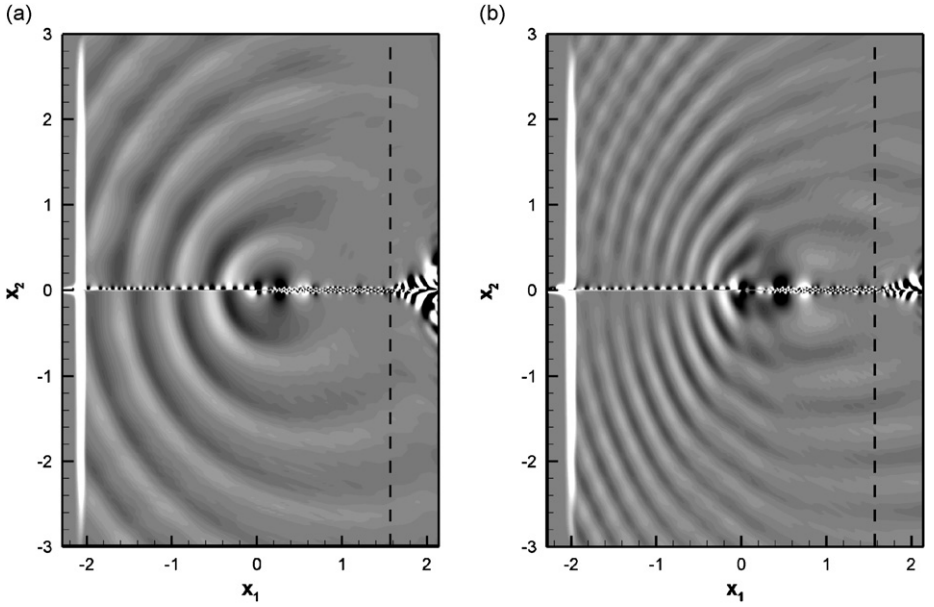

Fig. 4. Contours of dilatation obtained from DNS trailing edges with TS waves; $M = 0.4$, $\mu_0 = 9.57$, and $K_x = 54.34$ with contour levels $[-0.002; 0.002]$ (a); $M = 0.6$, $\mu_0 = 18.85$, and $K_x = 50.27$ with contour levels $[-0.003; 0.003]$ (b).

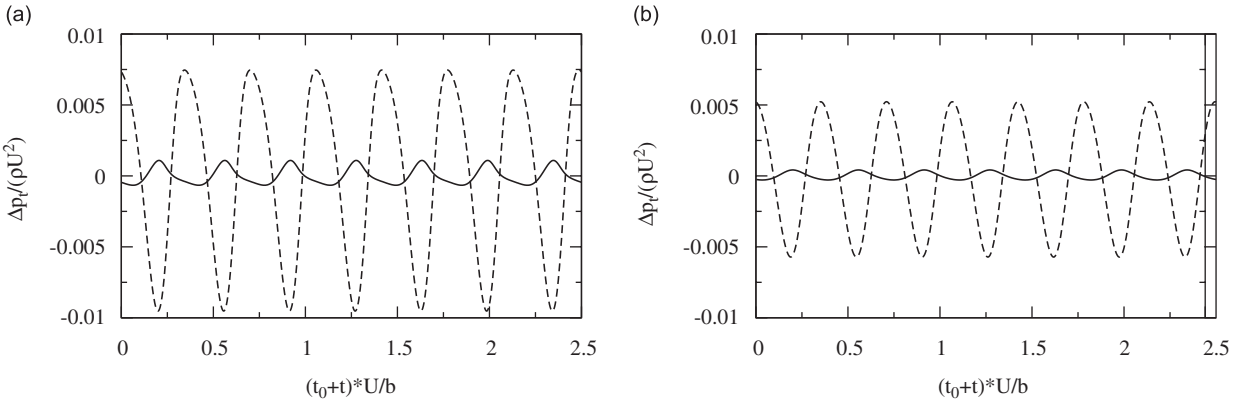

Fig. 5. Total pressure difference Δp_t from DNS for $M = 0.4$ (a) and $M = 0.6$ (b); (- - -) upstream of TE ($y_1 = -0.02$), (—) at TE ($y_1 = 0.0$), $\omega = 6.4\pi$.

5.1. Surface pressure jump transfer function H_S

The far-field pressure is evaluated as a function of the total pressure difference on the surface in both the 2-D and 3-D theory. Therefore, it is essential that an accurate representation of Δp_t is available. Amiet's theory relies on the surface pressure jump transfer function H_S to determine Δp_t. Therefore, this essential component will be the first subject of scrutiny. One of the key assumptions for deriving H_S is the validity of the unsteady Kutta condition at the TE [17]. Until today, there remains uncertainty regarding the accuracy of this premise for viscous flows [25]. Howe [26] demonstrates that the imposition of the Kutta condition results in a considerable reduction of sound generated by convection of disturbances past a TE. Here, the validity of the Kutta condition is investigated by analyzing the entire time-series of the surface pressure obtained from DNS.

Fig. 5 shows a time-series of the total pressure difference upstream of the TE and at the TE for both Mach numbers. At $y_1 = -0.02$, the total pressure difference oscillates with the forcing frequency $\omega = 6.4\pi$ and an amplitude of roughly 0.01 in both cases, indicating that the TS wave can still be considered a linear

disturbance. At the TE itself, the amplitude of Δp_t is considerably reduced for both Mach numbers. Considering that the Reynolds number in the present simulations is moderate, the unsteady Kutta condition appears to be a reasonable approximation even for viscous flows.

To assess whether the surface pressure jump transfer function H_S can correctly predict the total pressure difference, in spite of the unsteady Kutta condition not being exactly satisfied, the DNS were repeated extending the plate surface up to the outflow domain. Thus, simulations were conducted of the development of TS waves in a zero pressure gradient flat plate boundary layer. Due to the absence of a TE, no scattered pressure field was present and the simulations permitted recording the incident pressure field only. With the availability of p_i, Eq. (10) was applied in order to obtain p_t. Note that here only the total pressure on either side of the surface is computed, hence $p_t = [f_i + 0.5H_S]p_i$ for the top side (where TS waves are introduced) and $p_t = -0.5H_S p_i$ for the lower side.

The resulting magnitudes of disturbance pressure on top and bottom side of the surface are shown in Fig. 6 for simulations at $M = 0.4$. It can be observed that the incident pressure magnitude obtained from the boundary-layer DNS grows up to the TE location, i.e. in the flat plate boundary layer case the TS wave is amplified over the entire plate. Applying the surface pressure jump transfer function setting $f_i = 1$, good agreement with the total pressure obtained from the TE DNS is achieved in terms of frequency and phase, albeit the magnitude is slightly overpredicted in the vicinity of the TE. This is most likely caused by the fact that the TS wave in the TE simulation is subjected to a slight favorable pressure gradient just upstream of the TE. The growth is therefore reduced slightly such that the slope of the envelope of the incident pressure wave is reduced. To account for this change of the magnitude of p_i, the correction $f_i = 1 - 0.24\mathrm{e}^{0.07K_x y_1}$ is introduced. Making a better approximation of the 'true' incident pressure field the total pressure obtained by using Amiet's transfer function H_S matches closely that from the TE DNS. In fact the agreement is noteworthy, in particular for the phase, considering that H_S assumes the validity of the unsteady Kutta condition while the DNS data contains a non-zero value of Δp_t at the TE. For completeness, the total pressure was also computed using $f_i = \mathrm{e}^{\varepsilon K_x y_1}$ with $\varepsilon = 0.3$. A far too strong decay away from the TE can be observed, which was expected as the convergence factor was intended for a turbulent boundary layer and not TS waves in a laminar flow. Looking at total pressure on the bottom side of the plate (which only consists of the scattered pressure component) the magnitude of p_t obtained from H_S is again in good agreement with the TE DNS data.

Fig. 7 shows the magnitudes of disturbance pressure on the top and bottom sides of the surface for simulations at $M = 0.6$. Qualitatively the results correspond to those obtained at $M = 0.4$. It is particularly

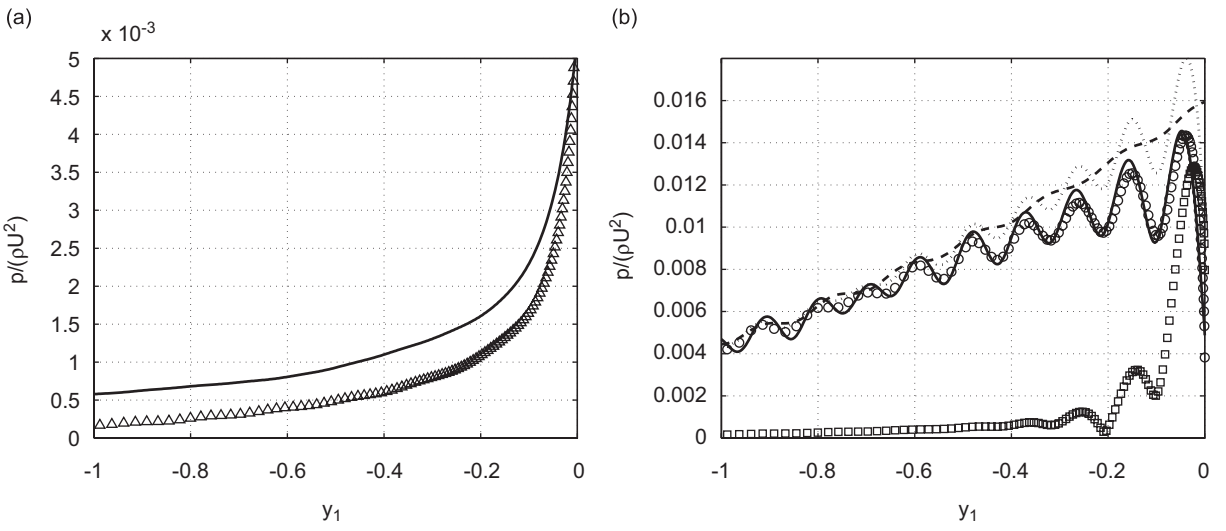

Fig. 6. Magnitude of disturbance pressure on top (a) and bottom (b) surface; (- - -) incident pressure p_i from boundary-layer DNS, (—) total pressure p_t from TE DNS, (···) $p_t = (1 + 0.5H_S)p_i$, (□) $p_t = (\mathrm{e}^{\varepsilon K_x y_1} + 0.5H_S)p_i$ [7], (○) $p_t = (1 - 0.24\mathrm{e}^{0.07K_x y_1} + 0.5H_S)p_i$, (△) $p_t = -0.5H_S p_i$; $\mu_0 = 8.38$, $K_x = 45.11$, and $M = 0.4$.

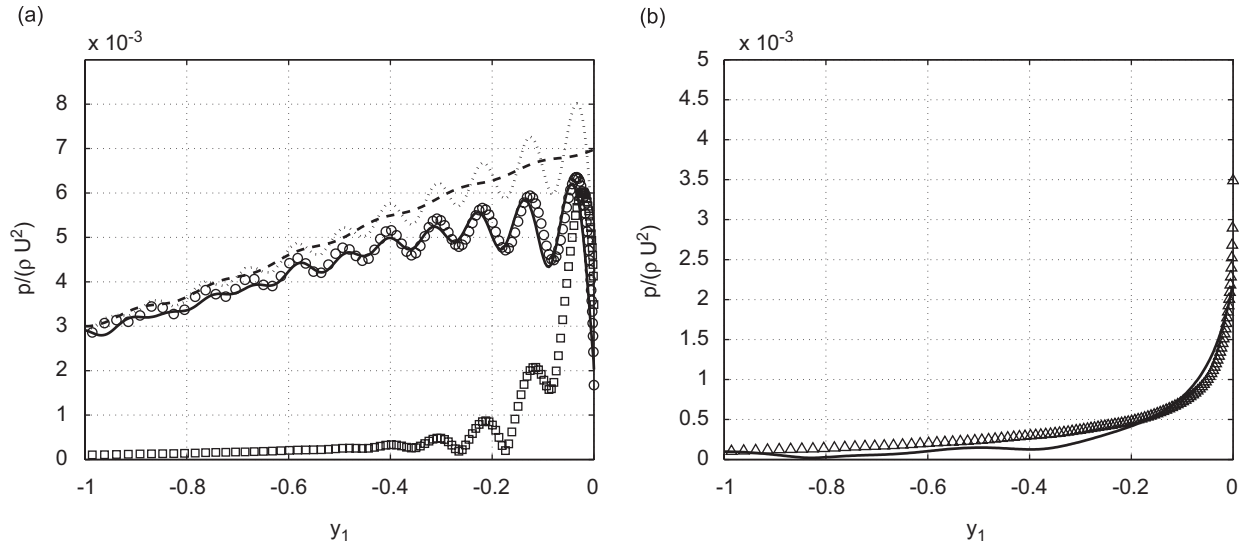

Fig. 7. Magnitude of disturbance pressure on top (a) and bottom (b) surface; (- - -) incident pressure p_i from boundary-layer DNS, (—) total pressure p_t from TE DNS, $(\cdots)$ $p_t = (1 + 0.5H_S)p_i$, (□) $p_t = (\mathrm{e}^{\mathrm{i}K_x y_1} + 0.5H_S)p_i$ [7], (○) $p_t = (1 - 0.24\mathrm{e}^{0.07K_x y_1} + 0.5H_S)p_i$, (△) $p_t = -0.5H_S p_i$; $\mu_0 = 16.49$, $K_x = 41.89$, and $M = 0.6$.

encouraging that good qualitative agreement with the TE DNS data can again be achieved using the same correction $f_i = 1 - 0.24\mathrm{e}^{0.07K_x y_1}$, especially for the phase. Overall it can be concluded that the surface pressure jump transfer function H_S performs well for different Mach numbers and reduced frequencies.

5.2. Acoustic pressure

Having shown that the total pressure difference on the surface can be predicted accurately using the pressure jump function H_S, the focus is now shifted to the acoustic pressure prediction. In one method the acoustic pressure p is evaluated using Eq. (6) where $\Delta p_t = p_{t_{\mathrm{top}}} - p_{t_{\mathrm{bottom}}}$, i.e. the difference of the top and bottom surface total pressures, from TE DNS. Alternatively, p is computed from Eq. (13) with $H_D = (1 - 0.24\mathrm{e}^{0.07K_x y_1} + H_S)$ using the incident pressure field from the DNS of a boundary-layer without TE. The results computed using 2-D theory are then compared to the acoustic pressure predicted by DNS. In DNS the acoustic pressure was obtained by conducting simulations over a period of at least four flow-through-times and computing p_{RMS}.

Fig. 8 shows the resulting acoustic pressure magnitudes at $R_d = 2$. For both Mach numbers, good agreement between the results using either Eq. (6) or (13) can be observed. This was expected considering that the surface pressure jump transfer function predicted Δp_t fairly accurately. Therefore, in both cases roughly the same surface pressure difference is radiated to the far field. However, comparing the results from 2-D theory with the acoustic pressure obtained directly from DNS appears to be more interesting. In order to obtain a reliable comparison, it is important to recognize the effect of the inflow sponge zone: the application of a volume force to generate TS waves causes a pressure peak on the top surface. The amplitude of the surface pressure difference at the disturbance location is considerably larger than in the vicinity of the TE. However, the disturbance generation was placed within the sponge zone in order to attenuate noise produced by the forcing. Thus the surface pressure difference within the sponge zone does not contribute to the far-field sound obtained directly from DNS. For this reason, only the pressure difference outside the sponge region is taken into account, i.e. the sources are integrated over the surface for $-2.0 \leqslant y_1 \leqslant 0.0$ according to Eq. (6) or (13). It should be noted that when including the surface pressure difference within the sponge zone, the magnitude of the acoustic pressure was considerably overpredicted, although the directivity was not changed significantly.

At $M = 0.4$ the agreement of the 2-D theory with the DNS data is good in terms of the location of the maxima and minima, in particular for the top surface. On the bottom surface, the DNS data curve appears

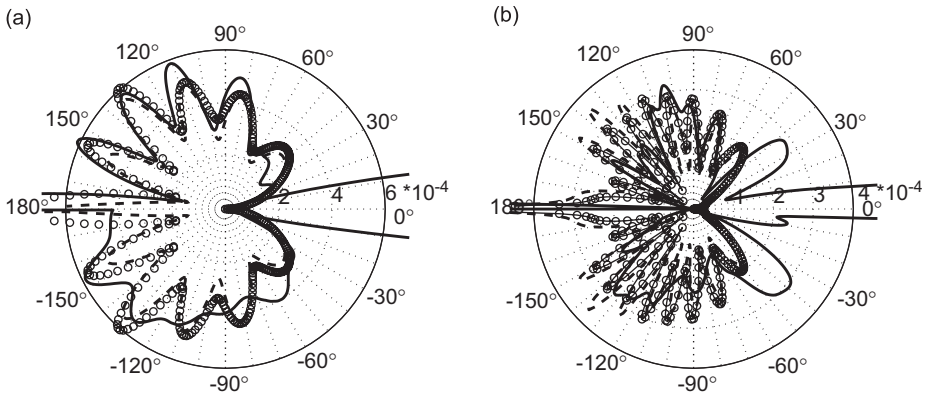

Fig. 8. Magnitude of acoustic pressure at $R_d = 2$ for $M = 0.4$ with $\mu_0 = 8.38$ and $K_x = 45.11$ (a), and $M = 0.6$ with $\mu_0 = 16.49$ and $K_x = 41.89$ (b); (○) $|p|$ from Eq. (13) using $H_D = (1 - 0.24e^{0.07K_x y_1} + H_S)$, (- - -) $|p|$ from Eq. (6) using $\Delta p_t = p_{t_{\text{top}}} - p_{t_{\text{bottom}}}$ from trailing edge DNS, (—) $|p|$ from DNS.

smoother, i.e. differences between minima and maxima are fairly small for the range $-140^\circ \leqslant \theta \leqslant -60^\circ$. This might be caused by the dissipating effect of viscosity, however an additional reason is discussed below. Similar behavior can be observed for the $M = 0.6$ case, albeit here significant additional downstream pointing lobes in the DNS data appear. The agreement of the upstream pointing lobes with 2-D theory also is not as good as in the lower Mach number case although the general trend is captured reasonably well. The current results have also been compared to additional calculations employing a far-field assumption. The amplitudes of the acoustic pressure were found to be similar regardless of whether the far-field approximation was made or not. However, the near field has a significant effect on the phase, i.e. when employing the far-field assumption the lobe structure of the DNS data could not be predicted accurately.

In order to potentially uncover the origin of the discrepancies between the DNS data and results obtained from 2-D theory, TE DNS were conducted without forcing. The main difference between theory and the DNS is not only the presence of boundary layers on the plate surface, but also, as mentioned previously, an unsteady wake downstream of the TE. The acoustic pressure was again obtained by calculating p_{RMS} over a period of at least four flow-through-times. The magnitude of acoustic pressure at $R_d = 2$ from the unforced DNS at $M = 0.6$ is shown in Fig. 9. In the absence of the forcing on one side of the surface, the resulting pressure pattern is symmetric with respect to $x_2 = 0$. A dominant lobe is visible pointing in the upstream direction and a secondary lobe is present which is inclined in the positive x_1-direction. This implies that significant noise is generated by the wake in the DNS simulation. The large value of the upstream pointing lobe most likely causes the smoothness of the DNS data shown in Fig. 8, as the TE noise is superposed with the wake noise. However, the magnitude of the secondary lobe is far too small to be the origin of the pronounced downstream pointing lobes seen in the forced DNS cases. To shed some light on what might cause these dominant lobes, the unsteady wake is scrutinized. The structure of the unsteady wake can clearly be identified when looking at vorticity contours (shown in Fig. 9). The wake remains steady for a long distance (up to $x_1 \approx 0.5 \approx 83\delta^*$). A Kelvin–Helmholtz (K–H) type instability leads to amplification of disturbances in the wake and a subsequent shedding of vortices. The spacing of the vortices in the resulting vortex street is highly regular, i.e. a dominant frequency is present. On the other hand, when looking at the wake of the DNS with TS wave at $M = 0.6$ (Fig. 9c) several significant differences can be detected. The wake becomes unsteady much farther upstream ($x_1 \approx 0.3 \approx 50\delta^*$). The reason is partly that the shear layer is perturbed with a larger amplitude (the TS wave) than in the unforced case. More importantly, the vortex street does not look as regular as in the unforced case. This is due to the fact that two separate frequencies are now present, the forcing frequency and the shedding frequency. The superposition of the TS waves with the K–H instability waves in the wake leads to vortex packets convecting downstream. Once the amplitudes of the disturbances become sufficiently large, nonlinear interaction can generate low frequencies that can radiate into the far field [27].Looking at contours of dilatation (Fig. 9) it appears as if the above described phenomenon is indeed

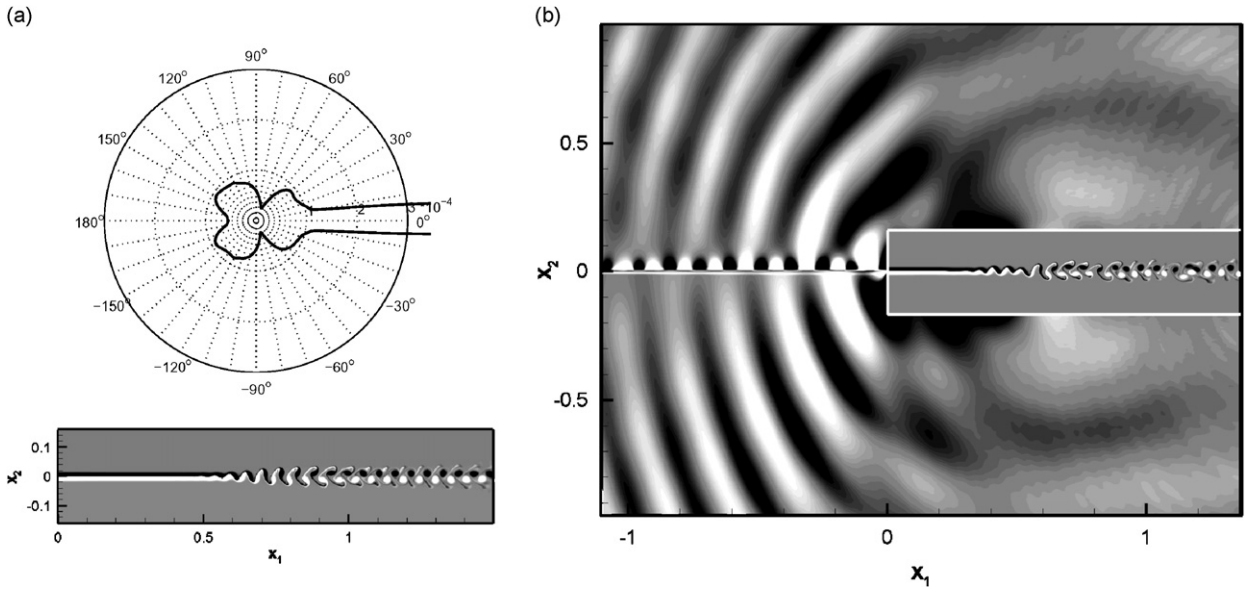

Fig. 9. Magnitude of acoustic pressure at $R_d = 2$ (a) and contours of vorticity $[-3; 3]$ (b) from unforced DNS of trailing edge; contours of dilatation $[-0.001; 0.001]$ with an insert of contours of vorticity $[-3; 3]$ (c) from DNS with $\mu_0 = 16.49$ and $K_x = 41.89$; $M = 0.6$.

responsible for sound generation in the wake. Clearly, acoustic waves originate at $x_1 \approx 0.7$, the location where shedding occurs, i.e. where the disturbances in the wake become nonlinear. These acoustic waves can be seen in Fig. 4b to propagate downstream at an angle that corresponds to the angle of the additional lobes found in the directivity plots. It is therefore suggested that the downstream pointing lobes are caused by nonlinear sound generation in the wake. The fact that the additional lobes were only observed at the higher Mach number can most likely be explained by observing that the additional source in the wake should be quadrupole-like according to the acoustic analogy. Therefore, the TE noise will be dominant at low Mach number.

Additional DNS of TEs were performed specifying slip walls [28], thus eliminating the unsteady wake downstream of the TE and, hence, the K–H instability waves. The slip wall simulations did not exhibit the pronounced downstream pointing lobes of Fig. 9, corroborating the above findings that these lobes are a consequence of nonlinear interaction between the K–H and the TS instability waves. It should be noted that the additional noise generation mechanisms might be enhanced by conducting 2-D simulations because only two distinct harmonic waves are present. In fully 3-D simulations, the boundary layer and the wake are turbulent and nonlinear interactions will most likely occur for many frequencies, albeit at lower amplitudes.

6. Summary

2-D DNS of an infinitely thin TE were conducted at $M = 0.4$ and 0.6. TS waves were introduced close to the inflow boundary to produce pressure fluctuations on the surface, generating TE noise. The aim of these simulations was to evaluate Amiet's theory. The original theory was modified to account for the radiation of the total pressure difference in 2-D only. In addition, no far-field approximation was made in the derivation of the 2-D theory.

The magnitude of the acoustic pressure in the far field obtained from the 2-D theory is larger than in Amiet's original theory due to the confinement of the radiation to a plane. For very low Mach numbers the directivity is similar to 3-D theory in the far field, however, for increasing Mach number the radiation in the downstream direction gains in significance relative to the 3-D theory. The DNS revealed that the unsteady Kutta condition is not exactly satisfied but constitutes a reasonable approximation for viscous flows. Despite having been derived assuming the unsteady Kutta condition to hold exactly, the surface pressure jump transfer function was shown to perform well for different Mach numbers and reduced frequencies.

The strictly 2-D theory was applied to numerically obtain the acoustic pressure as a function of the surface pressure obtained from DNS. Several differences appeared when comparing the results to the acoustic pressure directly computed by DNS. Firstly, the magnitude of the acoustic pressure computed by DNS is lower than that predicted by theory. This can most likely be attributed to viscosity, in particular to the presence of boundary layers. Secondly, the individual lobes computed by 2-D theory appear to be smeared in the DNS. Unforced DNS of TEs suggest that in addition to viscous effects, noise generated by the wake is partly responsible for smearing the lobes. Finally, high amplitude downstream pointing lobes can be observed in the DNS. Circumstantial evidence was presented that these lobes are caused by nonlinear sound generation in the wake.

Acknowledgments

This work was supported by the DTI under the MSTTAR DARP programme. Computer time was provided by the EPSRC grant GR/S27474/01.

References

[1] M. Lighthill, On sound generated aerodynamically I. General theory, *Proceedings of the Royal Society of London, Series A: Mathematical and Physical Science* 211A (1107) (1952) 564–587.
[2] M. Lighthill, On sound generated aerodynamically II. Turbulence as a source of sound, *Proceedings of the Royal Society of London, Series A: Mathematical and Physical Science* 222 (1148) (1952) 1–32.
[3] N. Curle, The influence of solid boundaries upon aerodynamic sound, *Proceedings of the Royal Society* 231 (1955) 505–514.
[4] J. Ffowcs Williams, L. Hall, Aerodynamic sound generation by turbulent flow in the vicinity of a scattering half plane, *Journal of Fluid Mechanics* 40 (4) (1970) 657–670.
[5] M.S. Howe, A review of the theory of trailing edge noise, *Journal of Sound and Vibration* 61 (3) (1978) 437–465.
[6] T. Brooks, T. Hodgson, Trailing edge noise prediction from measured surface pressures, *Journal of Sound and Vibration* 78 (1) (1981) 69–117.
[7] R. Amiet, Noise due to turbulent flow past a trailing edge, *Journal of Sound and Vibration* 47 (3) (1976) 387–393.
[8] E. Manoha, C. Herrero, P. Sagaut, S. Redonnet, Numerical prediction of airfoil aerodynamic noise, AIAA Paper 2002–2573, 2002.
[9] B. Singer, K. Brentner, D. Lockard, G. Lilley, Simulation of acoustic scattering from a trailing edge, *Journal of Sound and Vibration* 230 (3) (2000) 541–560.
[10] C. Seror, P. Sagaut, C. Bailly, D. Juvé, On the radiated noise computed by large-eddy simulation, *Physics of Fluids* 13 (2001) 476–487.
[11] D. Bodony, S. Lele, Spatial scale decomposition of shear layer turbulence and the sound sources associated with the missing scales in a large-eddy simulation, AIAA Paper 2002–2454, 2002.
[12] R.W. Paterson, P.G. Vogt, M.R. Fink, C.L. Munch, Vortex noise of isolated airfoils, *Journal of Aircraft* 10 (5) (1973) 296–302.
[13] R.H. Schlinker, R.K. Amiet, M.R. Fink, Vortex noise from nonrotating cylinders and airfoils, AIAA Paper 76–81, 1976.
[14] E. Nash, M. Lowson, A. McAlpine, Boundary-layer instability noise on aerofoils, *Journal of Fluid Mechanics* 382 (1999) 27–61.
[15] M.E. Goldstein, *Aeroacoustics*, first ed., McGraw-Hill, New York, 1976.
[16] D.G. Crighton, Basic principles of aerodynamic noise generation, *Progress in Aerospace Sciences* 16 (1) (1975) 31–96.
[17] R. Amiet, High-frequency thin airfoil theory for subsonic flow, *AIAA Journal* 14 (8) (1976) 1076–1082.
[18] R. Amiet, Effect of the incident surface pressure field on noise due to turbulent flow past a trailing edge, *Journal of Sound and Vibration* 57 (2) (1978) 305–306.
[19] F.M. White, *Viscous Fluid Flow*, McGraw-Hill, New York, 1991.
[20] M. Wei, J. Freund, A noise-controlled free shear flow, *Journal of Fluid Mechanics* 546 (2006) 123–152.
[21] N. Sandham, Y. Yao, A. Lawal, Entropy splitting for high-order numerical simulation of compressible turbulence, *Journal of Computational Physics* 178 (2002) 307–322.
[22] R.D. Sandberg, N.D. Sandham, Nonreflecting zonal characteristic boundary condition for direct numerical simulation of aerodynamic sound, *AIAA Journal* 44 (2) (2006) 402–405.
[23] M. Roger, S. Moreau, Broadband self-noise from loaded fan blades, *AIAA Journal* 42 (3) (2004) 536–544.
[24] H.F. Fasel, U. Konzelmann, Non-parallel stability of a flat-plate boundary layer using the complete Navier–Stokes equations, *Journal of Fluid Mechanics* 221 (1990) 311–347.
[25] D.G. Crighton, The Kutta condition in unsteady flow, *Annual Review of Fluid Mechanics* 17 (1985) 411–445.
[26] M.S. Howe, The influence of vortex shedding on the generation of sound by convected turbulence, *Journal of Fluid Mechanics* 76 (4) (1976) 711–740.
[27] N. Sandham, C. Morfey, Z. Hu, Nonlinear mechanisms of sound generation in a perturbed parallel jet flow, *Journal of Fluid Mechanics* 565 (2006) 1–23.
[28] R.D. Sandberg, N.D. Sandham, Noise due to unsteady flow past trailing edges, in: P. Wesseling, E. Oñate, J. Périaux (Eds.), *European Conference on Computational Fluid Dynamics, ECCOMAS CFD 2006*, 2006.